EE

# POLYTECHN
# IN2P3 -

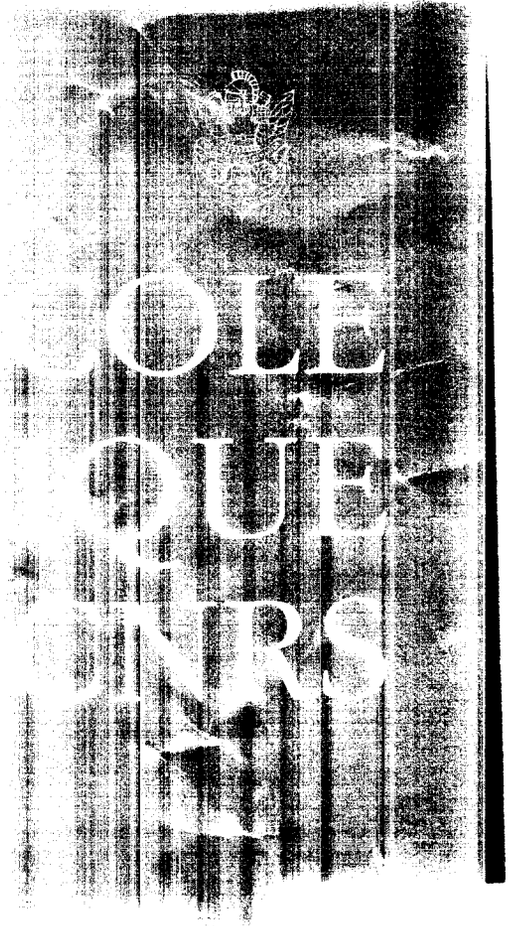


## Electron Acceleration in th
## Plasma Beat-Wave Experim
## at Ecole Polytechnique

*Contribution to the 6th Workshop on Ad*
*Accelerator Concepts*
*June 12-18 1994, The Abbey on Lake Geneva*

*Presented by D. Bernard*

X-LI

LABORATOIRE
DE PHYSIQUE
NUCLEAIRE
DES HAUTES
ENERGIES

91128 PALAISEAU
CEDEX - FRANCE

X-LPNHE 94/07
Sept 1994

# Electron Acceleration in the Plasma Beat-Wave Experiment at Ecole Polytechnique

*Contribution to the $6^{th}$ Workshop on Advanced Accelerator Concepts*
*June 12-18 1994, The Abbey on Lake Geneva, WI, USA*

*Presented by D. Bernard*

**X-LPNHE 94-07**

F. Amiranoff[1], J. Ardonceau[2], M. Bercher[3], D. Bernard[3], B. Cros[6], A. Debraine[3], J. M. Dieulot[3], J. Fusellier[5], F. Jacquet[3], J. M. Joly[5], M. Juillard[5], G. Matthieussent[6], P. Matricon[3], P. Miné[3], B. Montès[3], P. Mora[4], R. Morano[3], J. Morillo[2], F. Moulin[1], P. Poilleux[3], A. Specka[3], C. Stenz[7]

[1]LULI, [2]SESI, [3]LPNHE, [4]CPHT; all: Ecole Polytechnique, 91128 Palaiseau, France
[5]DSM-DAPNIA-SEA CEA Saclay, 91191 Gif sur Yvette, France
[6]LPGP, Université Paris Sud, 91405 Orsay, France
[7]GREMI, Université d'Orléans, 45000 Orléans, France

**Abstract**

Recent results of a plasma Beat-Wave acceleration experiment are presented. A plasma wave is created in a $D_2$ plasma by the beating of a Nd-YAG and a Nd-YLF laser pulse. Electrons at energies of 3 MeV are injected into the plasma. Several hundred electrons accelerated up to 3.7 MeV are observed in correlation with a Thomson scattering signal. The dependence of the electron acceleration on the plasma density demonstrates the beat-wave origin of the acceleration mechanism.

This paper is mainly devoted to the description of the experimental set-up. A particular attention was paid to efficient electron injection and to background noise suppression. A preliminary analysis of the results is also presented.

# 1 Introduction

Among new methods to accelerate particles by high electric fields, the beat-wave technique [1] has been investigated by several groups over the last decade. In this scheme two high-intensity laser pulses are focused in a gas and create a fully ionized plasma. The light intensity variation associated with the beating of the two laser waves provides a longitudinal ponderomotive force – which oscillates at the frequency difference of the two laser waves – on the plasma electrons. If this frequency difference is equal to the plasma proper frequency an electron plasma wave is resonantly created. The longitudinal electric field created by the charge separation of the plasma wave can reach up to several GV/m. The plasma wave amplitude grows with time until it saturates because of various possible mecanisms. A relativistic particle possessing the right phase can catch the wave and gain energy. An optimum effect is expected when the Lorentz factor of the plasma wave, determined by its phase velocity, is close to the Lorentz factor of the particle.

Recently it has been demonstrated that injected electrons could be accelerated up to several MeV, using a two-frequency $CO_2$ laser beam [2] with wavelengths of about 10 $\mu$m. Using the same technique, the acceleration of background plasma electrons has also been reported [3]. In these experiments the saturation of the plasma wave is attributed to relativistic de-tuning [4] and mode coupling with ion waves originating from stimulated Brillouin scattering [5].

In the experiment at Ecole Polytechnique presented here, a two frequency Neodymium laser with wavelengths of about 1 $\mu$m is used. In a first step, the plasma creation by multiphoton ionization of the gas by the laser was investigated [6]. Subsequently, the creation of the plasma wave by the beating of two laser pulses was studied [7]. In contrast to $CO_2$ laser experiments, the amplitude $\delta n/n$ of the plasma wave is limited here by modulational instability: the beat-wave-generated plasma wave couples to ion density perturbations and decays into two daughter electron waves. The measured value of $\delta n/n$ (1 to 5 %) has been found to be in agreement with model predictions (1.5%) of the maximum amplitude of the plasma wave in the presence of modulational instability [8]. This measured amplitude corresponds to an electric field between 0.3 and 1.5 GV/m.

After this optical study of the beat-wave generated plasma wave we have prepared the injection of electrons in the plasma. The new experimental set-up designed for

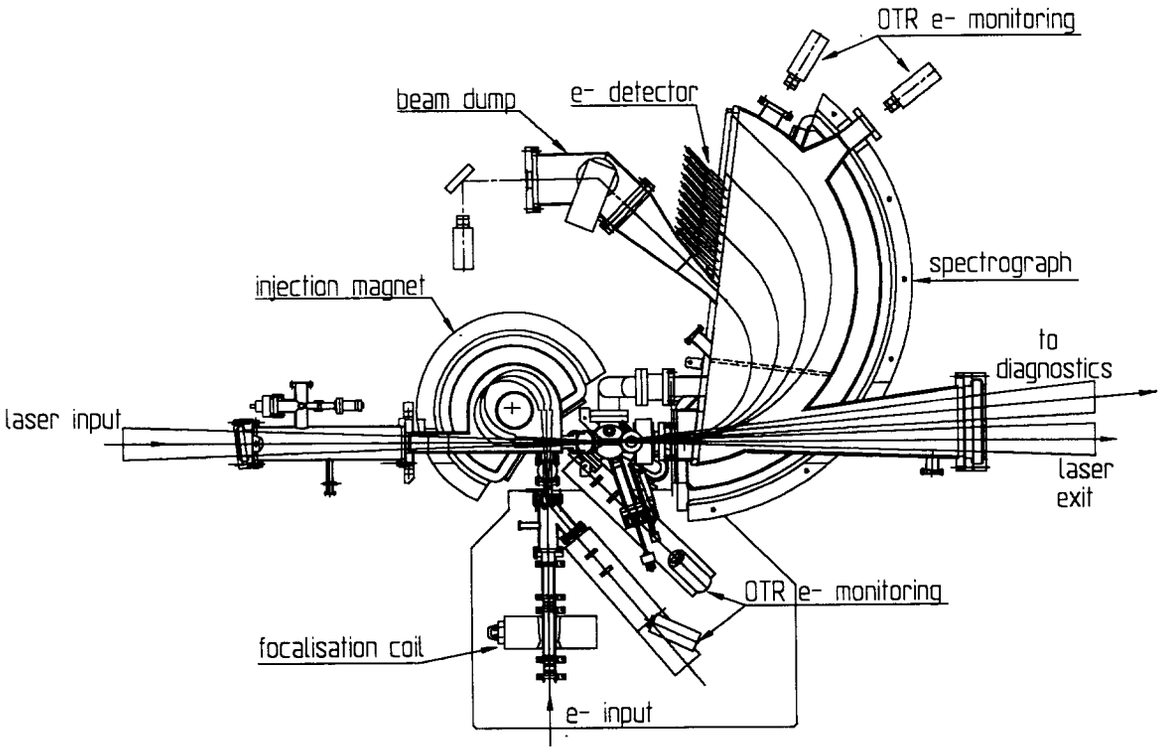


*Figure 1: The layout of the experimental set-up.*

that purpose is described in section 2. Beat-wave accelerated electrons have been observed recently and a preliminary analysis of the results is presented in section 3.

# 2 Experimental set-up

## 2.1 Overview

The lay-out of the experimental set-up is shown in fig. 1. A laser beam enters a gas vessel and creates a plasma at its focus. An electron beam is injected into the gas vessel through a thin aluminium window. It is then deflected and focused on the plasma by a double focusing achromatic $270^0$ dipole magnet with unit magnification. The electron spot is monitored at the entrance window and at the plasma location with high precision using optical transition radiation (OTR) imagery. The same monitor is used to align the relative positions of the laser and electron foci. A quadrupole-dipole magnetic spectrograph analyzes the accelerated electrons in momentum. These are then counted in a scintillator-PMT calorimeter hodoscope. The non-accelerated electrons are ejected to a beam dump.

## 2.2 Laser injection, plasma creation and optical diagnostic

The laser system is similar to the one used in preceeding experiments [7]. Two laser pulses delivered by a Nd-YAG and a Nd-YLF oscillator are amplified separately with a time delay of 1 ns in the laser chain of LULI up to an energy of 4.4±0.2 J and

11.8±0.4 J respectively, and with an output diameter of 90 mm. The YAG (YLF) pulse at 1.064 $\mu$m (1.053 $\mu$m) wavelength is 200±10 ps (90±10 ps) wide (FWHM). The quoted errors correspond to typical shot to shot variations within a series.

The experimental zone is located near the electron source and at a distance of about 190 m from the laser. In order to preserve the beam quality and stability, the laser beam is guided inside a vacuum pipe (0.04 mbar). An optical relay made of a pair of 50 m focal length lenses images the entrance window to the exit. The beam is steered inside the pipe by two pairs of motorized dielectric mirrors. The beam position can be monitored at eight different locations along the beam path. Each monitor is made of a removable cardboard reflector imaged by a CCD camera. The mirrors, the monitors and the vacuum system are remotely controlled by a single personal computer.

Profile and focal spot measurements did show that the beam quality is preserved in the transport. The short term (1 min) stability of the beam position at the focus of a 1.5 m focal length lens is of the order of 10 $\mu$m (RMS) which matches our needs. At larger timescales a slow drift of typically 0.1 mm/h is observed, which is probably due to thermal deformations of the buildings. Therefore, the laser beam is re-aligned between two successive shots.

The two pulses are synchronized in the experimental zone by means of rotating plates and polarizers. They are then focused by a 1.5 m focal length doublet lens and enter the gas vessel through a BK7 window. The focal spot is imaged with high magnification on a CCD camera and has a diameter of 60±20 $\mu$m (FWHM). The alignment system of the laser beam, of the electron beam, and of the plasma wave diagnostics is different from the one used in previous experiments [9] and is described in section 2.6.

About half of the energy is present in the central spot and the peak intensity is close to $10^{15}$ W/cm$^2$ which is much larger than the ionization threshold. Thus, the gas is fully ionized by multiphotoionization [6], and the initial electron density of the plasma is equal to twice the molecular density. The resonant electron density is $1.07 \cdot 10^{17}$ cm$^{-3}$, corresponding to a deuterium pressure of 2.187 mbar at 22$^0$C.

In contrast to previous experiments [7], we observe here the Thomson scattering of the incoming near-infrared laser light on the plasma waves at 5$^0$ [8]. A system consisting of a spectrograph, a streak camera and a CCD camera gives a time and frequency resolved measurement of the light scattered by the plasma wave. The unshifted laser light is blocked in front of the spectrograph by an interference filter and in its analysing plane by a neutral density. Thus only one of the Thomson scattering satellites is observed.

## 2.3 Electron source

The electrons with a kinetic energy of 2.5 MeV are provided by a Van de Graaff accelerator, ordinarily used for solid state physics. As we want to inject a small pencil of test electrons into a plasma of about 0.1 mm in diameter, we have characterized the beam with high precision using OTR monitors (cf. 2.6). This study has led to several modifications of the electron line. In particular, the energy of the beam

oscillates slowly over several seconds with a peak to peak amplitude of about 10 keV, leading to an inadmissible beating of the electron beam of 2 mm. Therefore, a new dispersionless beam line has been designed and installed.

We have also discovered that the alternative magnetic field created by the motor driving the belt of the Van de Graaff deflects the beam at a frequency of 50 Hz. As this deflection occurs at some distance of the filament, it appears as a rotation of the beam in the transverse plane at subsequent waists with an amplitude of a fraction of a millimeter. Magnetic shielding of the motor reduces the amplitude of the rotation by one order of magnitude. The residual movement is suppressed by pulsing the electron source at 10 Hz with an adapted phase locking. The pulse duration can be varied and is set to 0.4 ms with a maximum intensity of $315 \pm 15$ $\mu$A. During the experiment the laser shot was fired on the rising slope of the electron pulse at an intensity of about 200 $\mu$A. The measured emittance $\epsilon$ of the electron beam — defined as the product of the RMS beam size and the RMS divergence at a location of zero correlation — is equal to 0.06 mm·mrad.

## 2.4 Injection of the electrons into the gas vessel

The gas vessel with a $D_2$ pressure of about 2 mbar has to be separated from the vacuum in the beam pipe ($10^{-6}$ to $10^{-5}$ mbar) by a thin window. This affects low energy electrons who undergo important elastic scattering on their way through matter.

The passage through the entrance window has two main effects. Firstly multiple low angle scattering increases the beam divergence and hence affects the injection into the plasma. This also implies several inconveniencies for the design of the whole experimental set-up. In particular the air gap of the magnets must be large, and their aberrations must be further minimized. Secondly single large-angle scattering creates a halo around the "gaussian core" which may generate considerable background noise in the detector. The reduction of background noise is a primary concern in this experiment because the time constant of the detector (5 ns) is much larger than the duration of the signal, which is of the same order of magnitude as the lifetime of the plasma waves estimated to $40 \pm 20$ ps from the duration of the Thomson scattering signal.

For these reasons we paid particular attention to the choice of the window material and thickness. Because of the very high irradiation dose rate on the window (3 MGy/ms with a focused beam), a metallic foil has to be used. We chose aluminium for its low atomic number and because it can be easily mounted vacuum tight. The thickness is chosen as a compromise between the porosity of the foil and its pressure resistance on the one hand, and electron scattering considerations on the other. The porosity of thin aluminium foils is mainly due to the presence of micro-holes. Therefore, their permeability is by many orders of magnitude larger than the ordinary gas-through-metal diffusion permeability and increases very rapidly with decreasing thickness. The measured gas conductance through a 1.5 $\mu$m thick foil (Ø 4 mm) is lower than $10^{-7}$ l/s, providing a tolerable relative pression drop rate smaller than $5 \cdot 10^{-6}$ per hour.

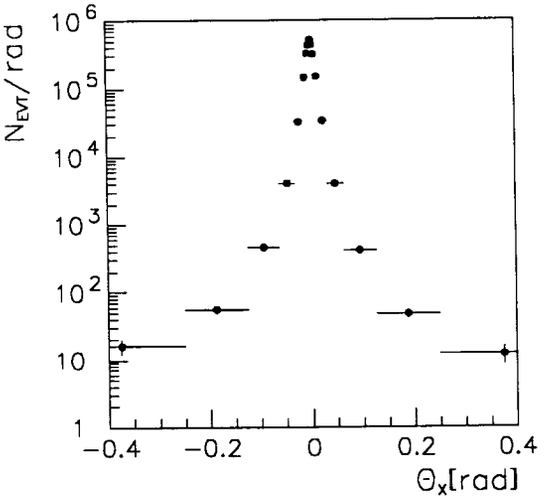


*Figure 2: Distribution of the scattering angle (horizontal plane).*

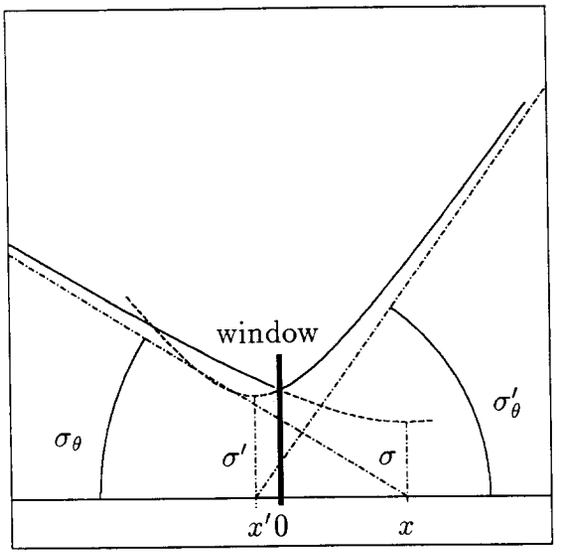


*Figure 3: Focusing on the entrance window (see text).*

**Scattering of the electrons by the entrance window**

Multiple scattering of charged particles traversing matter is usually described by the Molière formula [10] which gives the RMS of the gaussian core of the scattering angle distribution: $\theta_0 = 13.6\ \mathrm{MeV}/(\beta{\cdot}c{\cdot}p)\sqrt{t/X_0}[1 + \frac{1}{9}\log_{10}(t/X_0)]$. The formula has been fitted on experimental data [11] and is valid in the range $10^{-3} < t/X_0 < 100$ [12], where $t$ is the thickness of the window and $X_0$ the radiation length of the material.

The window thickness envisaged here is of the order of one micron ($t/X_0 \approx 10^{-5}$). In order to check the validity of the multiple scattering approximation, we compute the mean number of collisions per unit length $n = \sigma_c{\cdot}\rho{\cdot}N_A/A$. Here, $\sigma_c$ is the total elastic cross section[13]: $\sigma_c = 4\pi Z(Z+1)(\alpha a_0/(\beta Z^{\frac{1}{3}}))^2$, $a_0$ is the Bohr radius and $\rho, A, N_A, Z, \beta$ have their usual meaning. For aluminium ($n = 3.8\ \mu\mathrm{m}^{-1}$), we are in an intermediate regime called plural scattering. The plural scattering of the electrons by the window is studied using a Monte-Carlo simulation (fig. 2). The width of the angular distribution is estimated from the angle which contains 68% of the events ("68%-width") and is equal to 8.9 mrad whereas the Molière value is 8.7 mrad, and the measured value is $7 \pm 1$ mrad.

The large angle behaviour can be described by the "one large event" approximation: after integration over the azimuthal angle, the scattering angle distribution after the window can be written: $p(\theta) = 2{\cdot}n{\cdot}t{\cdot}\theta_c^2/\theta^3$, where $\theta_c$ is the cut angle due to the screening of the electric field of the nucleus by the surrounding electrons ($\theta_c = 3$ mrad in Al). After integration we obtain the probability of a scattering angle larger than $\alpha$: $P(\theta{>}\alpha) = n{\cdot}t{\cdot}(\theta_c/\alpha)^2$. The fraction of electrons which will be intercepted by any aperture stop behind the window grows linearly with its thickness. For a 1.5 $\mu$m thick aluminium window, the fraction outside a cone with half apex angle of 60 mrad is thus calculated to be 1.3% in comparison to 1.5% as computed with the Monte-Carlo. For an incoming intensity of 200 $\mu$A, this number corresponds to $1.6{\cdot}10^4$ $e^-$/ns.

These simple considerations show that at collimation angles more than six times

the width of the angular distribution, still a huge number of the incoming electrons will be intercepted. An important fraction of these will undergo small angle scattering on the vessel walls and may create background noise in the detector. Therefore, an optimized collimation system has been designed to block this halo up-stream the detector (cf. 2.8).

**Focusing of the electron beam on the entrance window**

The increase of divergence of the beam due to the entrance window degrades the beam emittance. The blow-up of the emittance is minimized by a suitable design of the beam optics.

The angular divergence of the beam after the window is simply $\sigma'_\theta = (\sigma_\theta{}^2 + \sigma_D{}^2)^{\frac{1}{2}}$ where $\sigma_\theta$ and $\sigma_D$ are respectively the RMS angular divergence of the incoming beam and of the scattering angle through the window.

The width $\sigma'$ of the waist of the beam after the window (fig. 3) can be written: $\sigma' = [\sigma^2 + x^2\sigma_\theta{}^2\sigma_D{}^2/(\sigma_\theta{}^2 + \sigma_D{}^2)]^{\frac{1}{2}}$, where $\sigma$ is the width of the waist of the incoming beam and $x$ is the waist-to-window distance. Obviously the minimization of $\sigma'$ leads us to ajust the longitudinal position of the waist of the incoming beam on the window ($x = 0$), and we get $\sigma' = \sigma$. This corresponds to a beam emittance behind the window: $\epsilon' = \sigma'\sigma'_\theta = \sigma(\sigma_\theta{}^2 + \sigma_D{}^2)^{\frac{1}{2}}$, that is $\epsilon' = \epsilon(1 + (\sigma_D/\sigma_\theta)^2)^{\frac{1}{2}}$. We would then like to minimize the emittance blow-up by focusing the beam as strongly as possible on the window.

In the experimental zone a quasi-parallel beam with a width of about 1 mm is received and focused on the entrance window with a magnetic solenoid lens. The lens-to-window distance cannot be smaller than 317 mm due to space constraints. This implies that $\sigma_\theta \approx 3$ mrad and $\sigma \approx 20$ $\mu$m. Therefore, we may use the "thick window" approximation ($\sigma_\theta \ll \sigma_D$) and we obtain: $\sigma'_\theta \approx \sigma_D = 9$ mrad and $\epsilon' = \epsilon \cdot \sigma_D/\sigma_\theta = 0.18$ mm·mrad.

The $x$ dependence of the width $\sigma'$ of the beam waist after the window reduces to: $\sigma' = [\sigma^2 + x^2\sigma_\theta^2]^{\frac{1}{2}}$, so that the longitudinal focus position must be adjusted to better than $\delta_x = \sigma/\sigma_\theta = 7$ mm, which is easily is achieved even in presence of energy fluctuations. The precision required for the measurement of the size of the focal spot is of the order of $\sigma$ and is reached using the OTR beam monitors.

## 2.5 Injection magnet

After passing the window, the beam is brought on the laser axis by a bending magnet which at the same time images the entrance waist at the plasma. In order to obtain a stable spot, the magnet has to be non-dispersive (achromatic).

Instead of an achromatic magnet combination, we use a single "triple focusing" (i.e. stigmatic and achromatic) dipole magnet, in order to minimize the path of the electrons in the gas. The reason for this is that any electron scattered by a gas molecule between the entrance window and the plasma will be imaged outside the plasma.

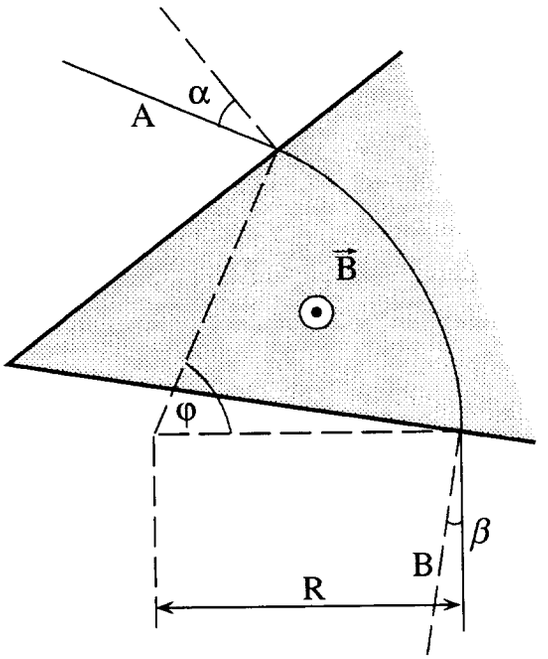


*Figure 4: Dipole parameter definition.*

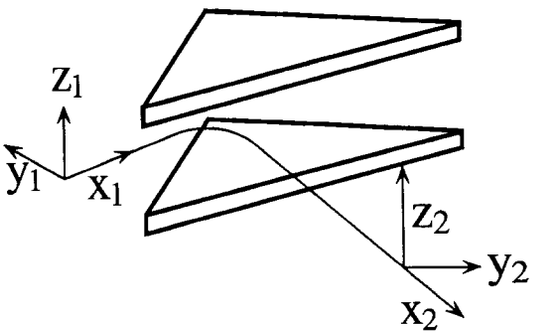


*Figure 5: Coordinate system.*

**Magnet calculation**

A homogeneous-field dipole magnet is usually described by the following parameters [14]: the length of the straight path before (after) the magnet $A$ ($B$), the radius of curvature $R$ of the electrons, the angle of the central ray with the entrance (exit) face of the dipole $\alpha$ ($\beta$), and the deflection angle $\phi$ (fig. 4). All quantities of dimension length can be normalized by the radius of curvature and are in this case denoted by a small letter, e.g. $a = A/R$. Hence the set ($a$,$b$,$\phi$,$\alpha$,$\beta$) defines a dipole magnet.

We introduce a coordinate system $(O_1, x_1, y_1, z_1)$ with its origin $O_1$ on the central ray, $x_1$ being the direction along the central ray, $y_1$ orthogonal to it and in the median plane, and $z_1$ perpendicular to that plane (fig. 5). A similar system $(O_2, x_2, y_2, z_2)$ is defined on exit. The median plane of the magnet is often called the horizontal plane, and $(O, z)$ the vertical direction. The angles are written $y'_1 = \mathrm{d}y_1/\mathrm{d}x_1$, and the momentum deviation $\mathrm{d}p/p$ is denoted $\delta$. In the paraxial approximation the coordinates and angles of a particle on exit are linear functions of its entrance coordinates and angles. The elements of the transfert matrices are written in the short form: $(y|y) = \mathrm{d}y_2/\mathrm{d}y_1$.

In this notation, a triple focusing magnet is described by the system of equations: $[(y|y') = 0\ ,\ (z|z') = 0\ ,\ (y|\delta) = 0]$; where each matrix element depends on the five parameters defining the dipole. The two remaining free parameters can be chosen to be the ratio of the two arms $g = a/b$ and $\phi$.

Solving of the system of equations leads to a second degree polynomial equation in $a$ [15]. At fixed positive $g$ the equation has one physical ($a > 0,\ b > 0$) solution for $232^0 > \phi > 180^0$ and two physical solutions for $360^0 > \phi > 232^0$. The two sets of solutions correspond respectively to magnets having either none or only one intermediate focal point in the horizontal plane.

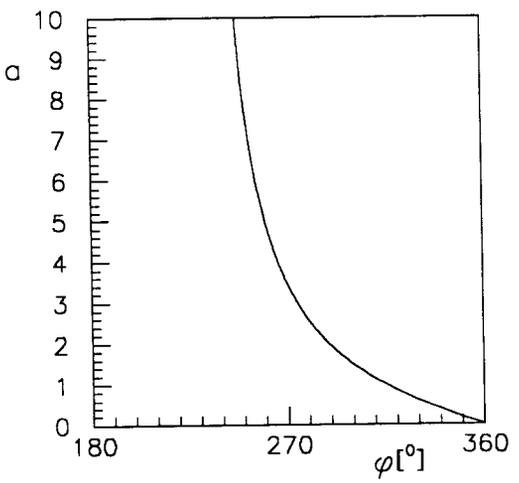


*Figure 6: Variation of $a$ with $\phi$ ($g = 1$).*

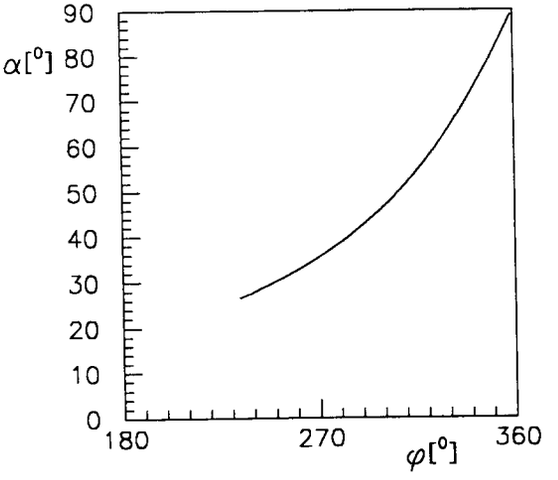


*Figure 7: Variation of $\alpha$ with $\phi$ ($g = 1$).*

The spot size on the entrance window is well matched to the plasma width. Therefore, we choose $g = 1$ and we obtain a symmetrical magnet with $a = b$, $\alpha = \beta$ and unit magnification in $y$ and $z$. With the choice of $\phi = 270^0$ we get reasonable values of $a$ and $\alpha$ (fig. 6 and 7). This also minimizes the second order aberrations and allows an easy implementation in the lay out. Solving the equation we obtain $a = b = 2$ and $\alpha = \beta = \arctan(1/2) = 26.6^0$.

The above results have been obtained in the limit of a small air gap. As mentioned before a magnet must in practice have a large air gap $H$, i.e. at least equal to $2 \cdot \theta_{\text{coll}} \cdot A$, where $\theta_{\text{coll}} = 60$ mrad is the collimation angle (cf. 2.8), i.e. $H > 0.24 \cdot R$. For mechanical reasons we had to use an air gap as large as $H = 0.6 \cdot R$. The shape of the fringe field has been computed with a program solving the Poisson equation [16]. Finally, the magnet was fine-tuned using a ray-tracing program [17] and we ended up with a still symmetric dipole magnet with $\phi = 270^0$, $a = b = 2.91$ and $\alpha = \beta = 33.2^0$ (fig. 8).

**Optical properties of the injection magnet**

The radius of curvature $R$ was chosen so as to minimize the increase of the size of the beam spot at the plasma due to elastic scattering in the gas. We can minimize this increase either by a reduction of the number of scatterings, or by a reduction of their effect at the plasma.

In hydrogen the value of the elastic parameters defined in (2.4) are $\theta_c = 1.3$ mrad and $n = 0.42$ m$^{-1}$ ( in 2 mbar of gas). The typical transverse position of a scattered electron at the plasma is $\Delta \approx A \cdot \theta_c$, and will be of the order of the size of the waist $\sigma'$ in absence of gas for $R \approx \sigma'/(a\theta_c) = 8$ mm which is obviously too small to be realized. The fraction of the electrons undergoing no scattering is $\exp(-(a + \phi + b)R \cdot n)$ which is smaller than 68% for $R < 0.1$ m. For this chosen value the typical transverse position of a scattered electron at the plasma is $\Delta = 260$ $\mu$m. The main part of the 32% fraction of electrons scattered form a large and low density — therefore invisible on the monitors — halo around the plasma. Yet when the scattering occurs close to

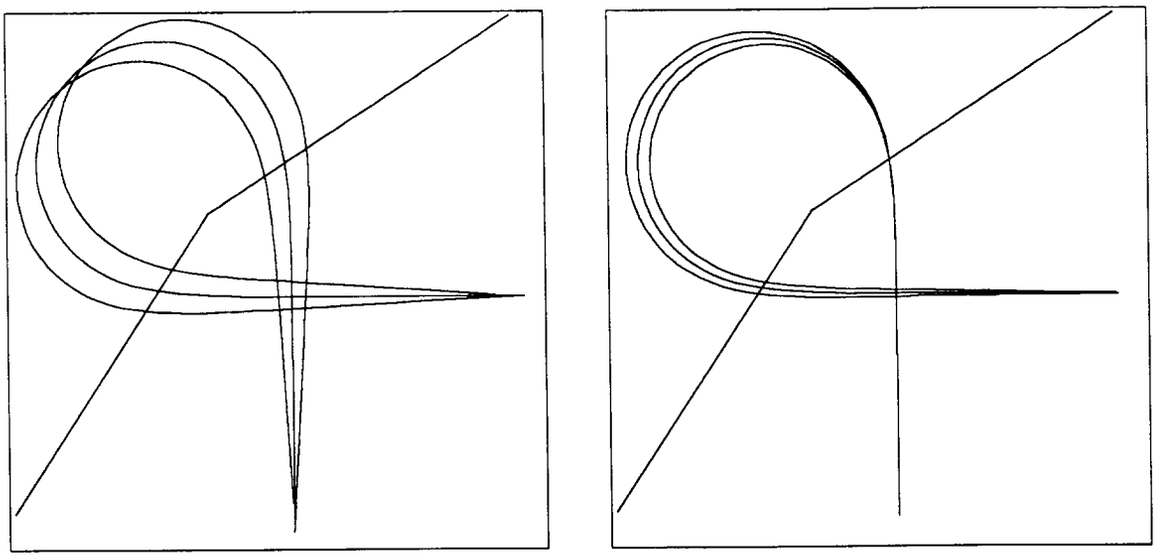

(a) Horizontal Focusing.

(b) Achromaticity.

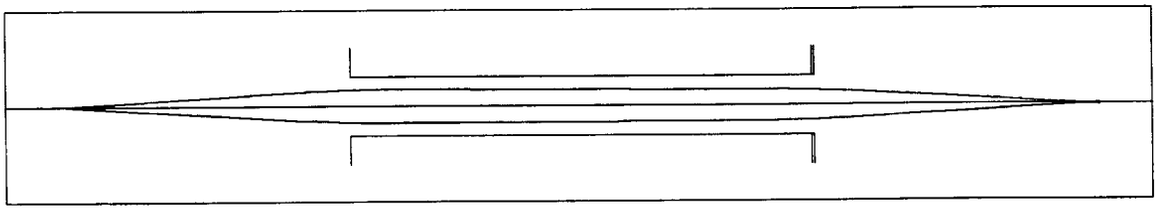

(c) Vertical focusing.

*Figure 8: Optical properties of the injection magnet. The marginal electrons are emitted at the collimation angle $\theta_{coll}$ (cf. 2.8) and at $\delta = \pm 0.05$.*

a waist, the position at the plasma can be rather small: these scatterings contribute to the width of the waist. The simulation shows that the 68%-width of the waist increases from 25 to 38 $\mu$m.

The aberrations of the injection magnet are dominated by the second and third order terms in the horizontal and vertical angles:

$$\delta_y = R{\cdot}(C_y^{02}{\cdot}z'^2 + C_y^{12}{\cdot}y'{\cdot}z'^2) \qquad \text{and} \qquad \delta_z = R{\cdot}(C_z^{03}{\cdot}z'^3 + C_z^{21}{\cdot}y'^2{\cdot}z'),$$

where the aberration coefficients are equal to $C_y^{02} = -0.7$ rad$^{-2}$, $C_z^{03} = -70$ rad$^{-3}$, $C_y^{12} = 51$ rad$^{-3}$ and $C_z^{21} = -44$ rad$^{-3}$.

The aberrations also create a halo of particles as far as 1.5 mm from the plasma (for a collimation at $\theta_{\text{coll}} = 60$ mrad) but their contribution to the width of the beam, computed from the 68%-width is only equal to 5.4 $\mu$m and 7.8 $\mu$m in the horizontal and vertical planes.

Due to the above effects the RMS width of the electron beam at the plasma is expected to be close to 40 $\mu$m.

**Beam test of the injection magnet**

During the commissioning of the magnet we have adjusted five parameters: the

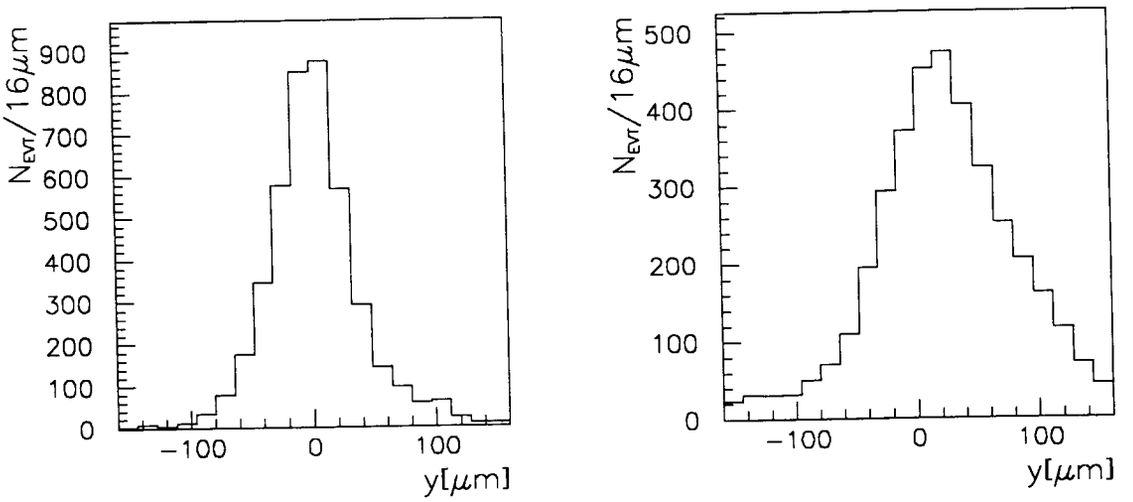


(a) vacuum.

(b) 2 mbar of hydrogen.

*Figure 9: The electron spot at the plasma location (horizontal plane).*

position and the angle of the beam in the horizontal plane, its focus in both vertical and horizontal planes at the plasma location, and the dispersion of the magnet. The adjustment has been realized by the variation of the following control variables: the position of the magnet in the horizontal plane, the magnetic field inside the magnet, the height of the field clamps, and the index of the magnet. The latter acts only on the stigmaticity of the magnet and can be remotely tuned in a small range ($\pm 2\%$) by the means of printed circuits carrying a current sheet.

The beam spot at the plasma is monitored by an OTR monitor. The typical values of the R.M.S. widths are 27 $\mu$m (H), 24 $\mu$m (V) in vacuum and 47 $\mu$m (H), 41 $\mu$m (V) in 2 mbar of hydrogen (fig. 9), and are compatible with the above estimations. The stability of the beam is of the order of 10 $\mu$m (RMS) which matches the needs.

## 2.6 Beam monitoring and alignment

The position and the size of the electron beam are measured in four different locations by beam monitors. These monitors [18] use the optical transition radiation (OTR) emitted by the electrons impinging on a metal surface (*radiator*) to image the beam spot on a CCD camera (fig. 10).

When a charged particle crosses the boundary between two media with different refractive indexes such as the surface of a metal window, it emits electromagnetic radiation. In the case of a metal-to-vacuum transition (forward TR) the emitted spectrum may range from the infrared to the soft X-ray domain, whereas in the inverse case (backward TR) the emission takes place mainly in the visible (OTR).

The backward emission is maximal on a cone centered on the direction of specular reflection of the electron with a half apex angle of $\gamma^{-1}$, where $\gamma$ is the Lorentz factor of the particle. This property permits easy observation of the beam at rather large angles. Therefore, the radiator is tilted by an angle $\psi$ with respect to the beam axis.

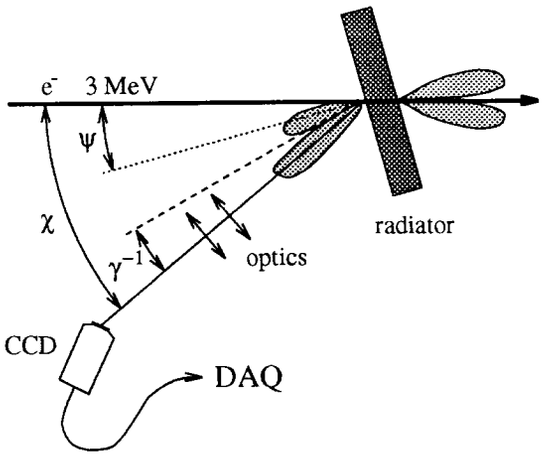


*Figure 10: OTR monitor (schematic).*

| # | $\psi$ | $\chi$ | $\lvert m \rvert$ | $t_0$ [mm] | NA |
|---|---|---|---|---|---|
| 1 | $15^0$ | $40^0$ | 1 | 200 | 0.093 |
| 2 | $17.5^0$ | $45^0$ | 1 | 260 | 0.090 |
| 3 | $17.5^0$ | $45^0$ | 1 | 200 | 0.093 |
| 4a | $37^0$ | $87^0$ | 1/34 | 760 | 0.011 |
| 4b | $37^0$ | $87^0$ | 1/25 | 300 | 0.017 |

*Table 1: Parameters of the beam monitors*

As the total photon yield is quite low (of the order of magnitude of the fine structure constant $\alpha$), the angle of observation $\chi$ is chosen at a maximum of emission. The working distance $t_0$ between the optical system with magnification $m$ and the metal surface is determined by available space.

The first monitor (cf. table 1) controls the beam size and position on the entrance window, which is used as the radiator. The second monitor views the beam spot at the plasma location. The radiator (13 $\mu$m Al foil) is mounted on a retractable target holder. The latter is also equipped with the secondary collimator of the upstream collimation system and with a silica prism used for the alignment of the Thomson-scattering diagnostic at $5^0$. The second monitor is used to adjust the relative positions of the electron focus and the laser focus. A third monitor with a radiator 3 cm behind the plasma location is used for angle measurements. The optical system and the camera are located above the median plane of the experiment and are thus omitted in fig. 1.

The functions of these three monitors require a high spatial resolution of the order of 10 $\mu$m, which is well matched to the pixel size of the CCD ($8 \times 16$ $\mu$m$^2$). This resolution has been achieved by using a symmetric optical system with unit magnification made up by two identical achromatic doublets. The computed value of the resolution, defined as the R.M.S. width of the point spread function, is in good agreement with the measured value (fig. 11). The points represent the measured values of the RMS width of the point spread function. At large apertures the spherical aberration dominates, whereas at lower apertures diffraction becomes important. (The diffraction limit is defined here as the RMS of the central peak of the Airy pattern for $\lambda = 500$ nm.) We use only the green part (480–560 nm) of the large OTR spectrum in order to make the contribution of the secondary chromatism negligeable.

When viewing the laser spot on the second monitor, we have to refocus in the near infra-red. For this purpose, the CCD camera is mounted on a motorized stage.

Two further monitors (4a and 4b) are used for the test and calibration of the electron spectrograph. We utilize the exit window (Al, 0.5 mm) as the radiator. The large viewing field is imaged with low magnification by ordinary TV lenses.

The sensitivity of the monitors can be defined by the current density of the

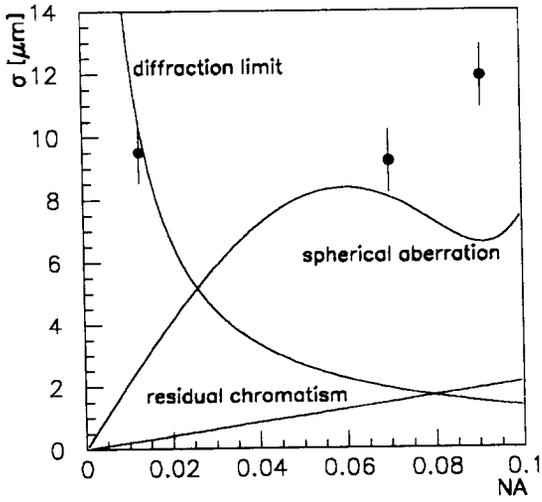


*Figure 11: The resolution of the first monitor as a function of numerical aperture (controlled by a diaphragm).*

faintest visible beam spot multiplied by the integration time of the CCD (20 ms). We measured a visibility threshold of 0.1 $\mu$A for a focused spot ($\sigma = 20$ $\mu$m) which gives a sensitivity of 0.8 $\mu\text{C}\cdot\text{mm}^{-2}$.

## 2.7 Magnetic electron spectrograph

The accelerated electrons are analyzed in momentum by a magnetic spectrograph. The design of the spectrograph was governed by a number of specifications. In particular, it must be broad-range (3–6 MeV/$c$) and stigmatic at 3 MeV/$c$. Furthermore, it must possess a high angular acceptance in order to match the high divergence of the accelerated electrons ($\approx$ 50 mrad (RMS), [19]). It must also have convenient geometrical properties, i.e. a straight focal line, a narrow "fan" of central rays and a reasonably low incidence angle on the focal line to permit a correct functioning of the electron detector.

We started out searching for an optimal dipole magnet and, for geometrical reasons, opted for an optically equivalent quadrupole-dipole (QD) combination, which then has been further optimized.

In order to assure an efficient ejection of the non-accelerated electrons, the spectrograph images the plasma (object point) to the entrance of the beam dump. The stigmaticity condition: $(y|y') = 0$ and $(z|z') = 0$ at $p = 3$ MeV/$c$ fixes the arms $a$ and $b$ of the dipole. Again, the resolution of the system of equations leads to a second order polynomial equation in $a$. We then restrict ourselves to "physical" dipoles ($a, b > 0$).

The demand for a suitable beam geometry has led us to consider the particular type of dipoles for which the (extended) exit face includes the entrance point (Fowler-Elbek dipoles [20]). For these magnets the deflection angle $\phi$ of the central ray does not depend on momentum and the fan of central rays is parallel on exit. This fixes the exit angle: $\beta = (\phi - \pi)/2$.

The remaining parameters $\alpha$ and $\phi$ are then adjusted within the permissible range of values so as to minimize the linear vertical astigmatism at momenta $p > 3$ MeV/$c$ and the incidence angle on the focal line. With a single dipole one cannot attain at the same time a low value of the entrance angle $\alpha$ and of the angle of incidence on

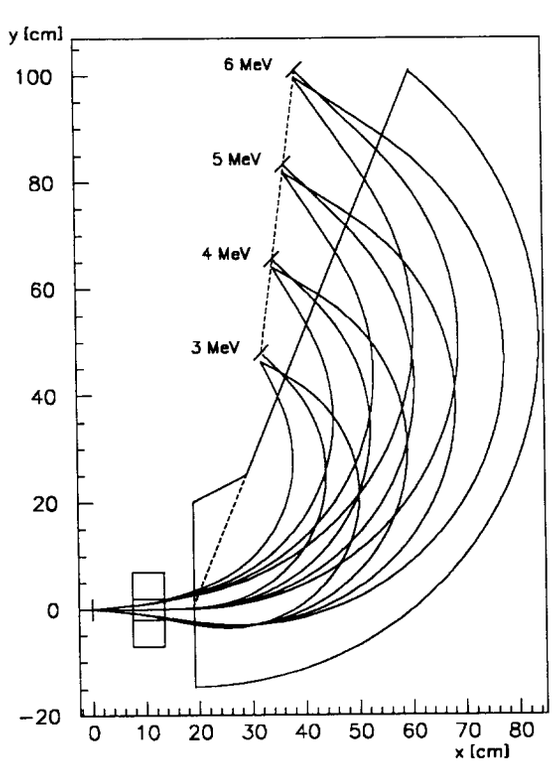


(a) horizontal ray-tracing.

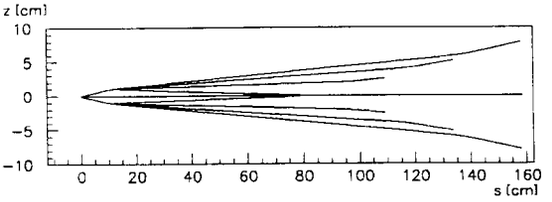


(b) vertical ray-tracing.

| quadrupole | | |
|---|---|---|
| length | | 60 mm |
| gradient | | 2.1 T/m |
| **dipole** | | |
| magnetic field | $B$ | 0.04 T |
| radius (3 MeV/$c$) | $R_0$ | 250 mm |
| air gap | $H$ | 100 mm |
| entrance angle | $\alpha$ | $0^0$ |
| deflection angle | $\phi$ | $136^0$ |
| exit angle | $\beta$ | $-22^0$ |
| focal line incidence angle | $\gamma_F$ | $37^0$ |
| horizontal magnification | | $-0.33$ |
| vertical magnification | | $-10$ |
| focal line sagitta | | 0.15% |

(c) numerical parameters.

*Figure 12: Magnetic electron spectrograph.*

the focal line $\gamma_F$. A large $\alpha$ is undesirable for magneto-optical reasons as well as for reasons of limited available space.

Therefore, the vertical focusing is accomplished by a quadrupole instead of an inclined entrance face of the dipole. The latter can be perpendicular to the central ray ($\alpha = 0$). The QD-combination was then further optimized for a finite air gap using a ray-tracing program [17]. Figure 12 shows the ray-tracing of the spectrograph in the horizontal and vertical planes for electrons of 3, 4, 5 and 6 MeV/$c$ and for marginal rays at $\pm 100$ mrad.

The dimensionless dispersion is defined by $d = (y|\delta) = (\partial y/\partial p)\cdot(p/R)$. For Fowler-Elbek dipoles we find $d = 1 - \cos\phi = 1.7$. The radius of curvature $R_0$ of the 3 MeV/$c$ electrons is chosen so as to reach a compromise between a low enough smallest detectable momentum and a reasonable length of the focal line. Between the entrance of the dump and the first scintillator exists a dead zone which cannot be smaller than 40 mm for mechanical reasons. For the chosen value of $R_0 = 250$ mm the smallest detectable momentum is equal to 3.27 MeV/$c$ and the length of the focal line (from 3 to 6 MeV/$c$) is equal to 54 cm.

At 3 MeV/$c$ the aberrations of the spectrograph are dominated by the second order terms in the horizontal and vertical angles:

$$\delta_y = R\cdot C_y^{20}\cdot y'^2 \qquad \text{and} \qquad \delta_z = R\cdot C_z^{11}\cdot z'\cdot y' \ ,$$

where the aberration coefficients are equal to $C_y^{20} = -4.0$ rad$^{-2}$ and $C_z^{11} = -4.4$ rad$^{-2}$.

The aberrations in the horizontal plane create a tail on the low energy side up to 8 mm from the central trajectory, as can be observed in the horizontal ray-tracing; in the vertical plane the tail extends to ± 10 mm. All these electrons enter the dump. The resulting (RMS) resolution of the spectrograph for a beam with a divergence of 50 mrad [19] varies from 33 keV/c (at 3 MeV/c) to 28 keV/c (at 6 MeV/c) and thus is well matched to the granularity of the detector (158 keV).

During the beam test of the spectrograph the beam has been scanned along the exit window by varying the magnetic field in the dipole. The measured RMS widths is 1 mm and 0.9 mm (at 10 mrad) in the y and z planes. The measured dispersion is compatible with the above calculation.

## 2.8 Collimation of stray electrons

We have seen above that the entrance window scatters a huge number of electrons at large angles and that many electrons undergo elastic scattering in the gas. Furthermore, electrons may be deflected by the radial electric fields generated by the plasma wave ([2], [19]). These electrons will eventually hit the walls of the chamber with a low incidence angle $i$ (fig. 13) and some of them will be back scattered.

The back scattering of electrons on a wall has been studied with the program EGS [21] which simulates the electromagnetic interactions of elementary particles in matter. At normal incidence ($i = 0$) we get a back scattering probability $f = 2.4\%$ (Al) and $f = 7.9\%$ (Fe). These numbers are lower than the experimental measurements $f = 5\%$ (Al) et $f = 14\%$ (Fe) [22] by a factor of two, probably because EGS uses the Molière approximation for multiple scattering. The back scattering probability increases drastically with increasing incidence angle (fig. 14), and almost reaches unity at grazing incidence (after the first Coulomb scattering the exit probability is already 50%). It should also be noted that the mean energy of the re-emitted electron increases and that its exit angle decreases with $i$. Many of these electrons will then propagate downstream in the chamber and eventually create background noise in the detector.

We have therefore designed a collimation system to block the halo electrons before they hit the walls. A primary collimator is installed behind the foil and intercepts the electrons scattered at large angle. An other – secondary – collimator is located at the subsequent waist of the beam – around the plasma – and blocks the electrons which have scattered on the edge of the primary. The scattering of electrons on the edge of a collimator has been studied in detail using EGS.

A collimator is a plate of thickness $e$ with a conical hole with angle $\xi'$ and input radius $R$ (fig. 15). The collimation angle $\xi$ is the angle of incidence of the electrons on the edge. The scattering skin depth of the edge is found to be a few tens of microns. Let $p(r)$ be the density distribution of the incident electrons on the front face of the collimator and $q(r)$ the probability of forward diffusion on the edge. Then the fraction of forward scattered electrons is $f = \int q(r)p(r)dr$. As $p(r)$ does not vary much over the thin skin depth, $f$ becomes $p(R)\int q(r)dr = p(R)\epsilon = 2{\cdot}n{\cdot}t{\cdot}\epsilon{\cdot}\theta_c^2/(d{\cdot}\xi^3)$, where $\epsilon = \int q(r)dr$ is an equivalent thickness. A quantity $\epsilon_0$ similar to $\epsilon$ is defined for electrons crossing the image plane at less than the radius of the secondary collimator

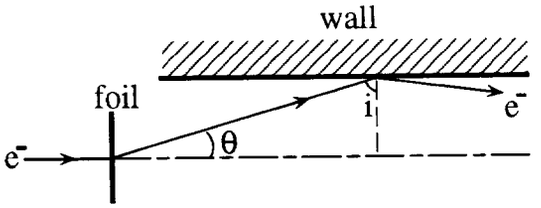


*Figure 13: Electron-wall scattering.*

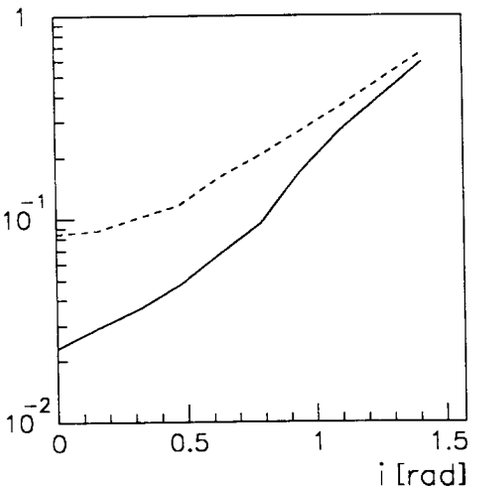


*Figure 14: Back scattering probability as a function of incidence angle (Al continuous, Fe dotted).*

(4 mm).

The values of $\epsilon$ and especially $\epsilon_0$ are very sensitive to the difference $\xi' - \xi$, which is called the freeing angle (fig. 16). For $\xi' < \xi$, the electrons are incident at low angles on the inner, conical surface of the collimator and exit by the same face: the collimator acts as a scatterer. However, when $\xi' > \xi$, the electrons are incident on the front face and the collimator is much more efficient, as expected. High $Z$ materials scatter out grazing electrons more efficiently and are thus favored.

A first "upstream" collimation system is installed before the plasma and cleans the beam after the entrance window. A "downstream" collimation system cleans the beam after the plasma.

### Upstream collimation system

A primary collimator is made of a 20 mm thick stainless steel plate with a collimation angle $\xi$ of 60 mrad and a freeing angle of 10 mrad. The forward scattered intensity from the edge of the primary collimator is about 300 $e^-$/ns. The secondary retractable cylindrical collimator with a radius of 4 mm is located in the image plane of the injection magnet, around the plasma. The outcoming intensity is then about 1 $e^-$/ns. As the horizontal magnification of the spectrograph is close to 1/3, these electrons end up in the beam dump (cf. 2.7, 2.10).

### Downstream collimation system

An other collimation system is installed downstream the plasma to block the electrons scattered at a large angles in the plasma.

The first collimator is located just in front of the quadrupole, shadowing its beam pipe. It has an elliptical hole in order to leave clearance for the Thomson scattering diagnostic at $5^0$. The collimation angle is 110 mrad in the vertical plane, 130 mrad

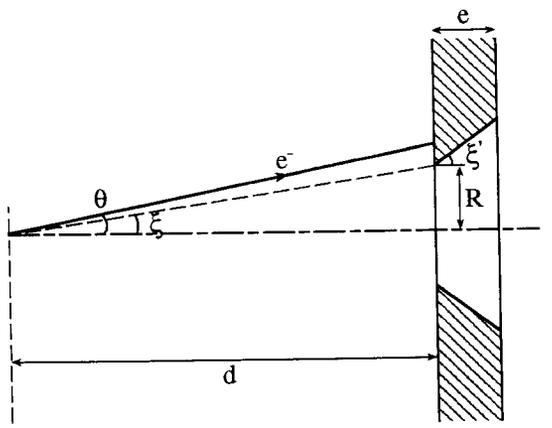


*Figure 15: Scheme of a collimator (see text).*

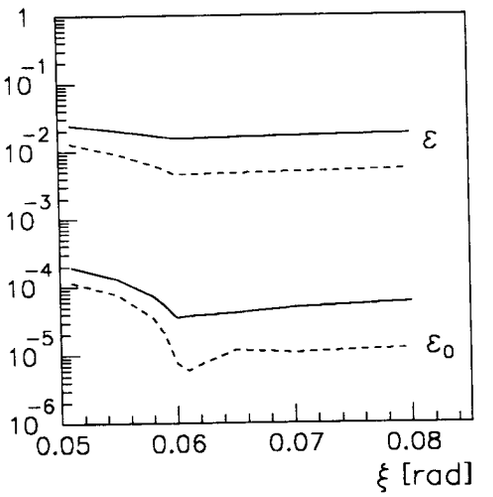


*Figure 16: The variation of $\epsilon$ and $\epsilon_0$ with $\xi'$ (Al continuous, Fe dotted).*

in the horizontal plane, and the freeing angle is 10 mrad.

The second collimator is located between the quadrupole and the dipole, with a geometrical collimation angle of 130 mrad and a collimator angle of 300 mrad. It provides an efficient cut in the horizontal plane because of the action of the quadrupole. For the same reason the cut depends on energy.

A third "slit" is located at an angle inside the dipole (fig. 1) and provides a cut at $\pm 15$ mm in the vertical plane. It blocks electrons of 5 to 6 MeV with a relatively large vertical angle (fig. 17), which would otherwise hit the horizontal walls of the chamber.

Note that when the retractable secondary collimator of the upstream system is removed the noise level in the detector is unchanged. Therefore the downstream system acts as an efficient secondary system of the upstream one.

The efficiency of the downstream collimation system has been tested by inserting the retractable foil at the plasma location. This blows up the electron beam to a 68%-width of 35 mrad and generates a wide halo. However, this increases the noise in the detector only by a factor of two.

**Angular acceptance**

The acceptance of the apparatus is limited by the downstream collimation system and by the height of the detector (fig. 17). We can see that the acceptance of the collimators at 3 MeV is larger than 80 mrad, i.e. larger than $\theta_{\text{coll}}$. Therefore, the downstream collimation system works safely in the shadow of the upstream one.

In the energy range of the detector the horizontal cut is close to 90 mrad, and the vertical cut is equal to 110 mrad at low energy (3.27–3.41 MeV), and then (3.41–4.84 MeV) decreases due to the limited height of the scintillators.

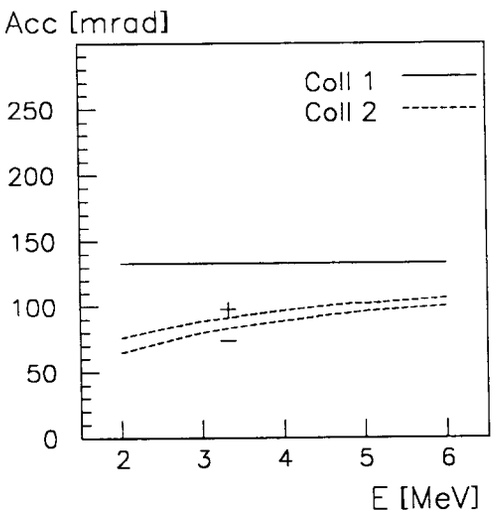


(a) Horizontal plane.

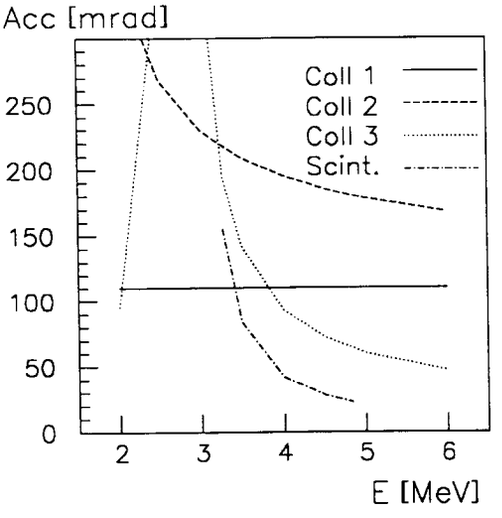


(b) Vertical plane.

*Figure 17: The angular acceptance as a function of the energy of the accelerated electrons. The cut in the horizontal plane is sligthly different depending on the sign of the angle (+,-) due to the fringe field of the dipole.*

## 2.9 Electron counter

The accelerated electrons are detected in a scintillator-photomultiplier (PMT) calorimeter hodoscope. The accelerated electrons impinge simultaneously on the scintillator and leave all their kinetic energy in it. The signal provides a measurement of the number of electrons in the burst.

The detector is an array of 10 scintillators of size $2 \times 2.2 \times 5.8$ cm$^3$, separated by 1 mm lead septa for containment. The positions of the axes of the scintillators correspond to an energy range from 3.34 to 4.77 MeV with a total energy range of 3.27 to 4.84 MeV.

The decay constant of the organic scintillator (NE111A) is 1.6 ns. The light is recorded by Hamamatsu R1635 photomultipliers, with useful photocathode diameter of 8 mm and a rise time of 0.8 ns.

The pulse heights are measured by CAMAC driven ADCs, triggered by the laser pulse. In order to take advantage of the short signal, 5 ns long linear gate modules are inserted between the PMTs and the ADCs; these are upgraded versions of linear gates originally developped for another experiment [23]. The time coincidence is adjusted by observing directly an attenuated light pulse from the laser on the photomultipliers.

The energy calibration of the detector is done by measuring cosmic muons, which deposit on average 4.4 MeV per event (fig. 18). This is cross-checked by observing the end spectrum of a $^{60}$Co gamma ray source and the 3 MeV electrons scattered by the gas. By varying the high voltage applied to the PMTs and using fast amplifiers, the dynamic range extends from one to a thousand electrons, 2.5 MeV kinetic energy equivalent each.

During the physics runs the PMTs were operated at 555 V, with signals of a few hundred millivolts, well below the impulse saturation level of the PMTs ($\approx$ 1.5 V).

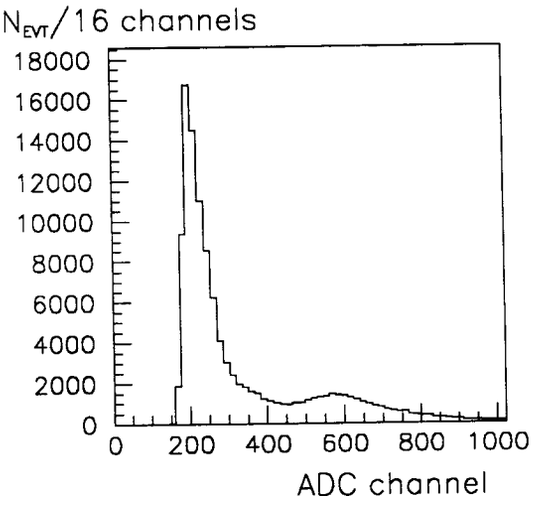


*Figure 18: Cosmic muon spectrum, with HV=900V and amplifier gain 14.*

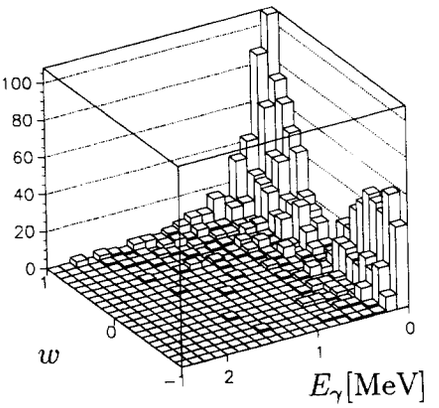


*Figure 19: $\gamma$ emission as a function of energy and of the cosine $w$ of the emission angle.*

## 2.10 Beam dump

As the life time of the plasma wave is rather short, only a small fraction of the incoming electrons are accelerated during the gated time interval. The non-accelerated electrons are directed into a beam dump where they are absorbed so as to generate as little as possible background noise in the detector.

The dump has the shape of a prismatic bottle (fig. 1) with a bottom made of low Z material (aluminium (0.9 mm) and water) in order to minimize the number of back scattered electrons (cf. 2.8), and backwards emitted hard $\gamma$ rays.

Most of the hard $\gamma$'s are emitted forward along the direction of the incident particles (fig. 19) and soft $\gamma$'s are easily blocked with a lead sheet. The remaining backward $\gamma$ rate is equal to 1.2 $ns^{-1}$ incident on each scintillator, and most of them will not interact in the detector.

The fraction of back scattered electrons from water is 0.8% over a solid angle of $2\pi$. With a simple bottle with a depth of 300 mm and a bottleneck area of 840 $mm^2$, 14 $e^-$/ns are re-injected into the chamber, and subsequently bent by the spectrograph into the detector. Moreover, low-angle back scattering of electrons off the side-walls of the dump may increase this rate. Preliminary measurements had shown that this source was dominating the noise in the detector (2–10 $e^-$/ns in one segment). A magnetic no-return device has then been installed (fig. 1), bending back scattered electrons into the side-walls of the dump. This reduces the noise level of back scattered electrons from the dump to less than 0.005 $e^-$/ns.

The Cerenkov light generated by the beam in water is viewed by a TV camera through a silica window and allows us to control the presence of the beam in the dump.

## 2.11 Background noise level

The background noise level is the sum of different contributions, the $e^-$ scattering in the gas, the $e^-$ back scattering and $\gamma$ retro-emission from the dump, the $e^-$ scattering and $\gamma$ emission on the edges of the collimators.

The sum of the four last contributions is measured under vacuum and is very small: a continuous electron beam of $0.1 \pm 0.01$ $\mu$A being injected in the vessel, the count rate at a discrimination threshold equivalent to 1 MeV is close to $2.5 \cdot 10^3$/s. This corresponds to a probability of $4 \cdot 10^{-9}$ and to a count rate of 0.005 $e^-$/ns at a beam current of 200 $\mu$A.

The remaining term is the noise due to the scattering in the gas. It is computed from the "one large event" approximation: $d^2p/(d\Omega \cdot ds) = n \cdot \theta_c^2/(\pi \cdot \theta^4)$. After a substitution of variables we obtain the density of probability per unit scintillator area as an integral over the curvilinear coordinate along the central trajectory $s$, containing elements of the transfer matrix from the scattering location to the image plane. The probability density is then integrated over $s$ and over the segment area.

The probability per segment decreases approximatively as the inverse of the fourth power of the dump-to-segment distance as in the small segment approximation. The corresponding count rate in the segment closest to the dump is then 0.17 $e^-$/ns.

The observed rate is larger: 2 $e^-$/ns ($p = 1.6 \cdot 10^{-6}$) per segment and increases slightly with the dump-to-segment distance. We believe that this gas-correlated noise is due to scattered electrons which impinge on the stainless steel flange constituting the entrance of the dump. A fraction of $6.1 \cdot 10^{-4}$ of the beam is scattered on the flange, 14% of these electrons are back scattered and the dipole bends them into the detector. This corresponds to a fraction of $8.5 \cdot 10^{-5}$, equal to fifty times the observed probability per segment, which seems reasonable.

# 3 Experimental operation and results

Before the experiment the chamber is evacuated to $10^{-7}$ mbar by a diffusion pump and afterwards filled with deuterium gas. The gas density is measured with a precision of $3 \cdot 10^{-3}$, and is stable within a relative variation of the order of $10^{-3}$ per day.

After an alignment of the beams a series of "shots" at 12 minutes interval is started. About a minute before each shot the positions of the electron and the laser spot at the plasma location are finely adjusted and recorded. For each shot the laser focal spots, energies, duration and YAG-YLF delay $\Delta t$ are also recorded.

The ADC measurements are acquired on a personal computer and stored. Channels 2 and 3 are also viewed on storage oscilloscopes. Pedestals are regularly recorded either with or without electrons.

The analysis of the data is still in progress and the complete results will be presented elsewhere [24]. We only present here the results of a pressure scan.

For this scan the PMTs are operated at 555 V, with calibration constants ranging from 1 to 3 electrons per ADC-count. The width of the pedestal of the first PMTs

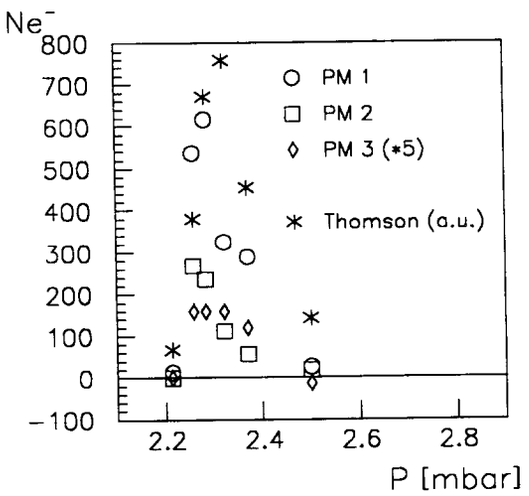


*Figure 20: Number of accelerated electrons as a function of the gas pressure (at $28.7^0 C$).*

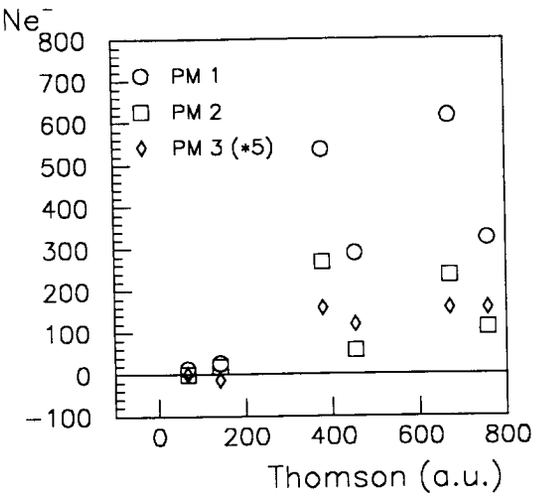


*Figure 21: Correlation of the electron signal and the Thomson scattering signal.*

is of about 2 ADC-counts, both with and without electrons. Therefore, the electron beam related background noise is negligeable compared to electronic noise (fig. 23).

The oscilloscope tracks show a beautiful single pulse above a very small noise. The correlation between the ADC and the oscilloscope measurements is excellent, which provides a cross-check of correct timing between the trigger of the linear gates and the signal of the PMTs.

**Results**

The pressure scan shows a narrow peak at the resonant pressure (fig. 20) which proves the plasma beat-wave origin of the signal (shots #31 to #39, three shots with inadequate $\Delta t$ being omitted). Furthermore, the electron acceleration signal is observed in correlation with the Thomson scattering signal (fig. 21).

The measured energy spectrum of accelerated electrons at $P = 2.284$ mbar is compared in fig. 22 to a 2D numerical simulation [19] with our experimental parameters. In this simulation the maximum amplitude is taken to be $\delta n/n = 1.6\%$ as deduced from the end-point of the observed energy spectrum.

In a first step the time dependence of the plasma wave is assumed gaussian with a FWHM of 40 ps as observed in the Thomson scattering studies. The simulated spectrum shows a sharp cut off at 3.7 MeV. The observed spectrum is clearly lower. The discrepancy is not due to an effect of acceptance limitation as the simulated angular divergence of accelerated electrons is small ($\approx$ 20 mrad) compared to the acceptance cut. However the discrepancy might indicate that the modulational instability destroys the coherence of the waves before they reach their maximum.

In a second step of the simulation we assume an amplitude ramping linearly with time (see fig. 6 in reference [8]). With a 10 ps ramp the simulation agrees with the experimental data.

A series of null tests was also done: shots with either no electrons, or no gas, or

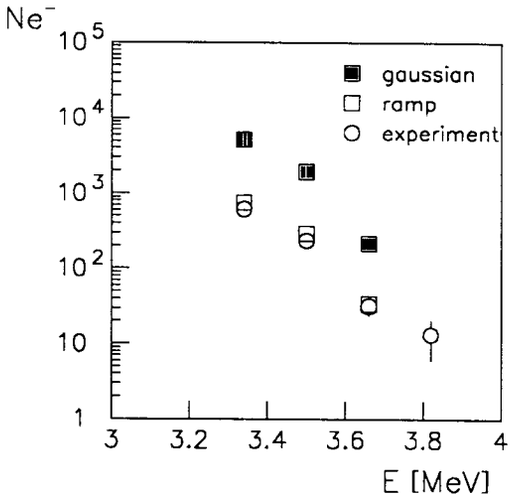


*Figure 22: Measured energy spectrum and simulation (shot #36).*

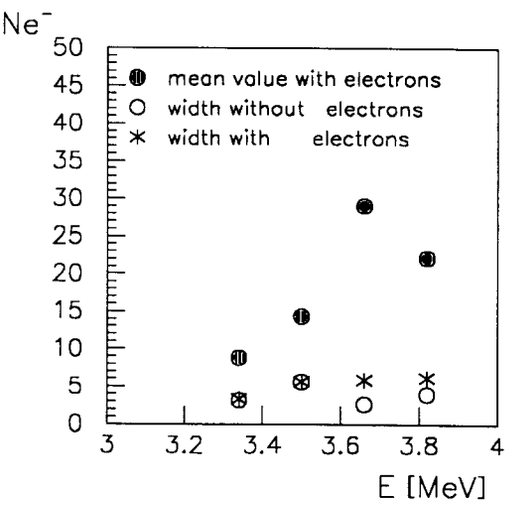


*Figure 23: Pedestal mean value (with $e^-$) and widths (with and without $e^-$) of the first channels.*

only one laser wavelength, or combinations of these. None of them did show a signal of accelerated electrons.

# 4 Conclusion

An experiment for the demonstration of the principle of beat-wave acceleration with a two-frequency Nd:glass laser has been presented. The two major design goals of the experimental set-up were the efficient injection of an electron beam of about 0.1 mm in size into a plasma (of about the same width) and the maximal suppression of background noise.

For this purpose an electron beam handling system with a stability and a precision of about 10 $\mu$m has been designed. The beam is monitored by OTR monitors with the same precision.

The reduction of background noise has governed the design of the injection magnet and of the electron spectrograph. It has led to the dedicated design of a two-stage collimation system, of an adapted beam dump, and to the use of fast detectors. The resulting $S/\sqrt{N}$ ratio reaches 200.

We have observed the acceleration of externally injected electrons by a relativistic plasma wave. This is the first evidence of plasma beat-wave acceleration with a two-frequency Nd:glass laser. The observed maximum energy gain of 0.7 MeV corresponds to a maximum plasma wave amplitude of about 1.6% which agrees with previous optical measurements. The maximum electric field is then 0.5 GV/m.

The acceleration length — determined by the depth of the laser focus — is close to its optimum value at our injection energy [25]. The plasma wave amplitude cannot be increased significantly by stepping up the laser energy because of saturation by modulational instability.

Two ways to increase the energy gain might by envisaged in the future:
- increase the injection energy and at the same time the acceleration length
- reach a higher plasma wave amplitude by the use of a short laser pulse (wakefield acceleration).

# 5 Acknowlegments

We gratefully acknowledge the help of the staff of the LULI, LPNHE and SESI during the experiment. We thank also M. Poitevin, S. Simon and Y. Fournier (DAPNIA) for their help with the modification of the electron beam line.

We also want to thank F. Méot (LNS) who has supplied us with his ray-tracing program, his assistance, and many invaluable hints on magnet design.

This work was financially supported by Ecole Polytechnique, IN2P3-CNRS, SPI-CNRS, CEA, EEC and DRET.

# References

1. T. Tajima and J. Dawson, Phys. Rev. Lett. **43** (1979) 267.
2. C.E. Clayton et al., Phys. Rev. Lett. **70** (1994) 37.
   C.E. Clayton et al., Phys. Plasmas **1** (1994) 1753.
   M. Everett et al., Nature **368** (1994) 527.
3. Y. Kitigawa et al., Phys. Rev. Lett. **68** (1992) 48.
4. F. Martin et al., New Developments in Particle Acceleration Technique, CERN preprint 87-11.
5. C. Darrow et al., Phys. Rev. Lett. **56** (1986) 2629.
6. J.R. Marquès et al., Phys. Fluids B**5** (1993) 597.
7. F. Amiranoff et al., Phys. Rev. Lett. **68** (1992) 3710.
8. F. Moulin et al., Phys. Plasmas **1** (1994) 1318.
9. F. Amiranoff et al., Rev. Sci. Instr. **61** (1990) 2133.
10. Review of Particle Properties, Particle Data Group, Phys. Lett. B **204** (1988)
11. V. L. Highland, Nucl. Instr. and Meth. **129** (1975) 497-499.
12. G. R. Lynch, O. I. Dahl, Nucl. Instr. and Meth. **B58** (1991) 6-10.
13. High energy particles, B. Rossi, Prentice-Hall Incorporated, NY, 1952.
14. Deflecting Magnets H. A. Enge, in "focusing of charged particles", edited By A. Septier, Academic Press, 1967.

15. D. Bernard, A. E. Specka, *in preparation.*

16. The CERN POISSON programe package (POISCR) Users guide, R.F. Holsinger, C. Iselin (available at CERN).

17. ZGOUBI Users' Guide, F. Méot, S. Valéro, SATURNE note LNS/GT/93-12 (1993).

18. A. Specka et al., proceedings of the IEEE Particle Accelerators Conference , pp. 2450-2452, Washington, D.C., 1993.

19. P. Mora, J. Appl. Phys. **71** (1992) 2087.

20. D. J. Prowse, W. .M. Gibson, J. Sci. Instr. **33** (1956) 159.
J. Borggreen et al., Nucl. Inst. and Meth. **24** (1963) 1.

21. The EGS4 code system, W. R. Nelson et al., SLAC-Report-265, December 1985.

22. G. Soum et al., Revue Phys. Appl. **22** (1987) 1189-1209, *in French.*

23. J.M. Dieulot et al., Nucl. Instr. and Meth. A**314** (1991) 185.

24. F. Amiranoff et al., *in preparation.*

25. A. E. Specka, Ph.D. thesis (*in French*), unpublished (1994).